Compensating Field-of-View Constraints for Decentralized Indoor Localization using Multi-Pose Techniques

Myoungsun Kim, *Graduate Student Member, IEEE*, Sirous Bahrami, *Member*, *IEEE* and Wonbin Hong, *Fellow, IEEE*

Abstract— **This paper presents an adaptive calibration method and compensation scheme to improve Direction of Arrival (DoA) estimation in decentralized indoor localization systems with resource-limited mobile tags. Traditional DoA methods require precise synchronization and complex hardware, unsuitable for large-scale use. Our Received Signal Strength Difference (RSSD)-based approach, featuring an adaptive calibration technique, corrects orientation-dependent errors, enhancing DoA accuracy. Simulation errors decrease from 12.5° to 1.01°, and real-world errors from 9.42° to 3.79°. We introduce: (1) a Refined Beam Shift Model to correct angle-induced errors, and (2) the Multi-Pose FoV Compensation (MPFC) scheme, which reduces RMSE by up to 60% using just two antennas, significantly simplifying hardware needs. The proposed method is scalable, efficient, and applicable to IoT-based localization and healthcare monitoring. Future research will explore real-time deployment and machine learning integration for further improvements.**

Index Terms— **Direction of Arrival (DoA), Indoor Localization, Decentralized systems, Received Signal Strength Difference (RSSD), Mobile Tag Localization.**

I. INTRODUCTION

I NDOOR localization has become a critical component of modern technology, enabling precise tracking and navigation in various applications. Beyond traditional navigation, it plays a key role in healthcare monitoring, logistics management, and smart Internet-of-Things (IoT) systems, where accurate position estimation is essential [1]. As localization applications continue to diversify, the need for scalability becomes increasingly critical. Consequently, supporting thousands of mobile devices per sensor anchor presents significant challenges, including RF congestion and interference among closely spaced tags [2]. Conventional centralized approaches struggle with scalability due to high communication overhead and computational demands. To address this, decentralized localization systems have been proposed as a more scalable and flexible solution [3], [4]. In decentralized localization, mobile tags perform their own position estimation rather than relying on a centralized server. Traditional localization techniques, such as Time-of-Arrival
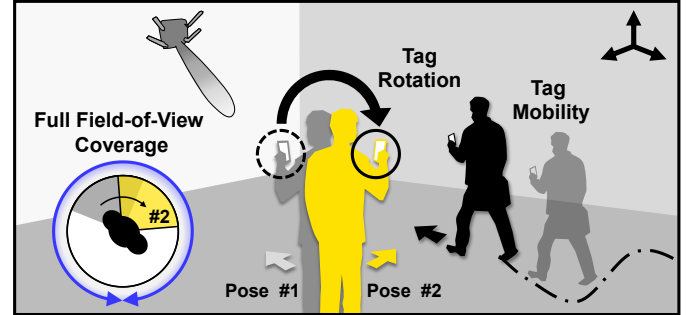

Fig. 1. A schematic of the proposed Multi-Pose Field-of-View Compensation Scheme, illustrating the characteristics of a mobile tag in an indoor environment.

(ToA) and Phase-Difference-of-Arrival (PDoA), require precise time synchronization and involve high computational complexity [5], making them impractical for resource-constrained mobile tags [6], [7]. Given the limited resources of mobile tags, it is essential to simplify the estimation process and optimize the supporting hardware while maintaining accuracy.

Received signal strength (RSS)-based approaches have been explored as a more hardware-efficient alternative, offering simplified computations with lower processing requirements [8], [9], [10]. However, conventional RSS fingerprinting and RSSI ranging [11] suffer from high localization errors in dynamic environments due to signal fluctuations caused by obstacles and moving objects. By focusing on relative values from multiple antennas rather than fragile absolute RSS values, RSS-based Direction of Arrival (DoA) methods improve resilience to environmental changes and mitigate multipath effects on RSS variation.

Beyond the system complexity, mobility itself introduces a significant challenge in implementing accurate decentralized localization systems. Distinct from static sensors, as shown in Fig. 1, mobile devices can move freely and change their orientation, making misalignment between the sensor node and the reference node inevitable. Research [12], [13] has shown that orientation misalignment leads to degraded DoA estimation accuracy. Moreover, RSS-based methods are particularly sensitive to tag orientation, as received power is heavily influenced by the radiation patterns of tag antennas. In [14], the degrading effect of misalignment is addressed within

The authors are with the Department of Electrical Engineering, Pohang University of Science and Technology (POSTECH), Pohang 37673, South Korea. (email: whong@postech.ac.kr)

AP2503-0890

decentralized RSS-based DoA systems; however, it has not been thoroughly analyzed.

Localization performance is bounded not only by accuracy but by the angular span over which that accuracy holds—the tag's Field-of-View (FoV). Conventional Directional arrays sharpen angular sensitivity but collapse FoV. State-of-the-art full-coverage systems therefore default to mechanical rotation or ≥8-element circular arrays [15], [16], pushing the tag footprint well beyond the form-factor of a phone or micro-UAV. While increasing the number of antennas can broaden the FoV [17] this often compromises the device form-factor. As an alternative to numerous antennas or mechanical rotators, frequency-scanning antennas using a frequency-hopping scheme have been introduced [18]. However, this scheme can cause interference on adjacent frequency channels, making it unsuitable for adaptable and versatile mobile devices.

To address the performance degradation challenges in mobile tag sensor applications, we introduce an innovative adaptive calibration framework, Multi-Pose Field-of-View Compensation (MPFC). This framework compensates for orientation-dependent errors and significantly expands the FoV, all while maintaining low hardware complexity by using only two antennas. Three key advancements are introduced to address FoV and accuracy limitations in dynamic environments:

- Anchor-Tag Misalignment Calibration: The impact of anchor and tag orientation variations on RSSD is analyzed, and the effect of gain variation on DoA estimation accuracy is identified. To mitigate the degraded DoA performance caused by misalignment, a new class of calibration method is proposed and validated through both simulations and experimental results across multiple orientations.
- Refined Beam Shift Model: Typically, a constant shift is assumed to simplify calibration, but this leads to errors when there is a large misalignment between orientations. To improve the accuracy of the system, this study develops more accurate models that account for changes in both the incident and orientation angles.
- Multi-Pose FoV Compensation (MPFC): MPFC leverages multiple tag orientations to refine DoA estimation, compensating for misalignment errors while achieving full angular coverage, as shown in Fig. 1. This approach overcomes the FoV limitations typically associated with small tags.

Through extensive simulations and real-world experimental measurements, this study demonstrates that the MPFC method effectively mitigates FoV constraints and enhances DoA estimation accuracy. Distinct from previous RSSD-based DoA methods that focused on fixed orientations, MPFC does not require additional hardware modifications or computationally expensive multi-antenna setups, making it a practical and scalable solution for real-world IoT deployments.

II. VERIFICATION OF ADAPTIVE CALIBRATION METHOD ON VARIOUS ORIENTATIONS

Accurate DoA estimation requires compensation for RSSD variations caused by tag movement. This section introduces a calibration method to address these variations by leveraging an RSSD-based approach and validates it across different anchor orientations in both simulations and experiments. Building on previous work in RSSD-based DoA estimation for mobile tags [19], this study introduces an RSSD-based approach that simplifies estimation by requiring only a single subtraction. Additionally, it employs a tilted array configuration with these two antennas—the minimal hardware necessary for RSSD operation—which reduces overall hardware complexity [9].

A. Compensating Anchor-Tag Misalignment

We assume Line-of-Sight (LoS) propagation and the far-field condition, ensuring that multipath effects are minimal [20]. Under these assumptions and the general scenario illustrated in Fig. 2, the received signal strength (RSS) of the n-th antenna in the tag, denoted as RSS_n^{dB}, can be expressed as follows:

$$RSS_n^{dB}(\theta_{inc}, \varphi_{inc}, D, \theta_{tilt}) = G_n^{dB}(\theta_{inc}, \varphi_{inc}) + P_n(D_n, \theta_{tilt}, \varphi_{tilt}) + w_n \quad (1)$$

where $G_n^{dB}(\theta_{inc}, \varphi_{inc})$ represents the gain pattern of n-th antenna in the expected direction of the target $(\theta_{inc}, \varphi_{inc})$. P_n is the incident power at the n-th receiving antenna, and w_n is the noise component, modeled as a zero-mean gaussian random noise variable.

The incident power P_n consists of three components: the transmitted power, the channel gain (with a typical path loss exponent $\eta = 2$) and the anchor antenna. It is formulated as:

$$P_n(D_n, \theta_{tilt}, \varphi_{tilt}) = P_T + \eta \cdot 10 \log\left(\frac{4\pi D_n}{\lambda}\right) + G_{T,n}(\theta_{tilt}, \varphi_{tilt}) \quad (2)$$

where $G_{T,n}(\theta_{tilt}, \varphi_{tilt})$ represents the transmitting antenna pattern as seen by the n-th receiving antenna and D_n denotes the distance between the anchor and n-th receiving antenna.

The angle θ_{tilt} denotes the misalignment angle between the anchor's boresight axis and the LoS path on the yz plane, as depicted in Fig.2. In (2), the incident power P_n varies not only with propagation distance D_n but also with the anchor-tag orientation misalignment angle θ_{tilt}. To simplify the analysis, we model the system in the yz-plane, setting the azimuth components (φ_{inc} and φ_{tilt}) to zero in (1) and (2). We validated this 2D simplification through simulations that introduced a height misalignment between the tag and anchor. The results confirm that the impact of this azimuth difference on DoA estimation is negligible, justifying our model.

Fig.3 illustrates the center displacement effect on channel gain and anchor gain variation. In the tilted array configuration, each antenna's phase center is offset by $y_I/2$ along the y-axis and by $z_I/2$ along the z-axis, as shown in Fig. 3. The mismatch in the phase centers of antennas in the tilted array affects both the transmitting gain and the channel gain of each antenna.
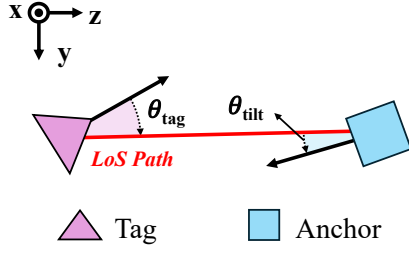
AP2503-0890

Fig. 2. Illustration of general DoA estimation scenarios considering the effects of anchor-tag orientation misalignment.
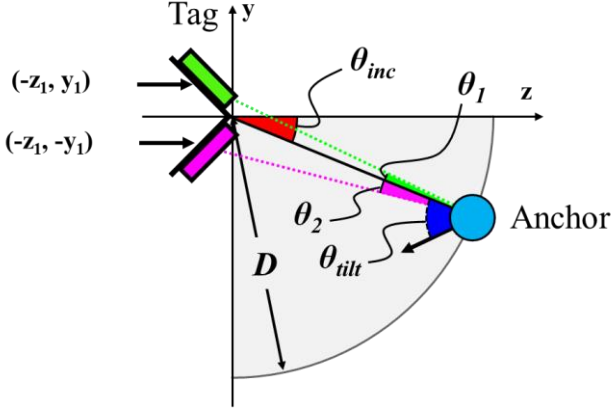

Fig. 3. A schematic illustrating the center displacement effect on channel gain and anchor gain variation. Antenna 1 is depicted in green, while Antenna 2 is shown in pink. Setting the center edge of the tilted array as (0,0), the centers of the tag antennas are represented as $(-z_1/2, y_1/2)$ and $(-z_1/2, -y_1/2)$, respectively

Distance variations across tag antennas have a negligible effect on RSSD variations, satisfying the far-field assumption ($D \gg y_1$ and z_1), while anchor gain variations significantly influence RSSD.

As illustrated in Fig. 3, the anchor gain variation can be represented by the transmitted beam shifted and is expressed as follows:

$$G_{T,n}(\theta_{tilt}) = G_T\left(\theta_{tilt} + (-1)^n \theta_n\right)$$
$$\cong G_T\left(\theta_{tilt} + (-1)^n \beta\right) \quad (3)$$

where G_T represents the transmitting gain pattern, which peaks in the direction of the LoS path. While the angular shift θ_n varies with the tag and anchor positions as well as θ_{inc}, it is approximated as a constant β in (3) for simplicity. By substituting the antenna gain expressions into the RSSD and applying (1) to (3), the final expression is derived as follows:

$$RSSD_c\,(\theta_{inc}, \theta_{tilt}) = RSS_1^{dB} - RSS_2^{dB}$$
$$\cong G_1^{dB}(\theta_{inc}) + G_T^{dB}(\theta_{tilt} - \beta)$$
$$- G_2^{dB}(\theta_{inc}) - G_T^{dB}(\theta_{tilt} + \beta)$$
$$= RSSD_{tag}(\theta_{inc}) + RSSD_{anc}(\theta_{tilt}) \quad (4)$$

In practice, the measured RSSD is obtained by averaging multiple received packets. This process significantly reduces the variance of the noise term w_n, which justifies the simplification of neglecting noise for the subsequent analysis [20]. The calibrated RSSD equation in (4) can be separated into
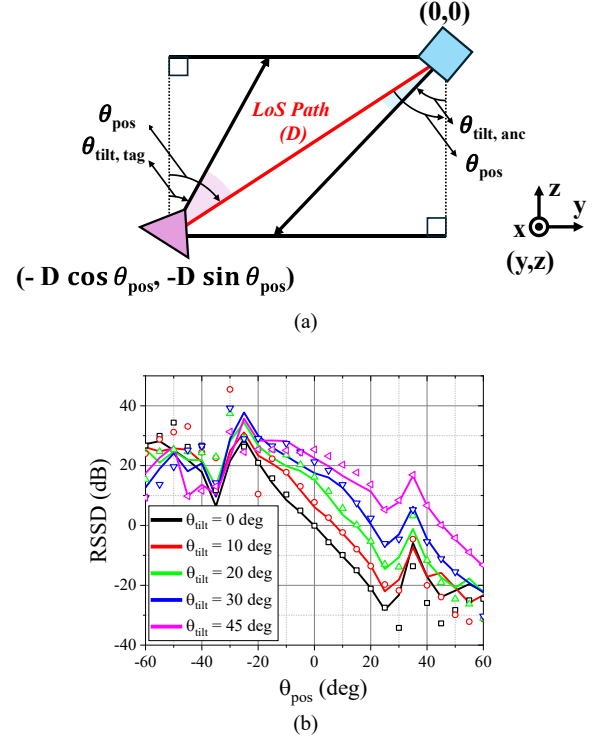

(a)

(b)

Fig. 4. (a) A illustration of the scenario with a mobile tag, introducing the positional angle θ_{pos} and orientation angles of each device, $\theta_{tilt,tag}$ and $\theta_{tilt,anc}$, respectively, as replacements for the incident angle θ_{inc} and θ_{tilt}, and (b) calibrated $RSSD_c$ obtained using (4) alongside $RSSD_m$ data for evaluation, derived from simulations imitating a moving tag, as shown in Fig. 4(a).

TABLE I. SIMULATION-BASED ESTIMATION ERROR: RMSE COMPARISON (CALIBRATION VS. NO CALIBRATION, WITHIN FoV)

Estimation Error (°)	$\theta_{tilt,tag}$				
	0°	10°	20°	30°	45°
w/ Calibration	1.01	5.35	3.57	4.58	5.74
w/o Calibration	12.31	11.68	18.65	26.87	39.48

two terms, each associated with a different angular effect: θ_{inc} and θ_{tilt}. Each effect can be represented as $RSSD_{tag}$ and $RSSD_{anc}$, respectively, where these components are defined as follows:

$$RSSD_{tag}(\theta_{inc}) = G_1^{dB}(\theta_{inc}) - G_2^{dB}(\theta_{inc}) \quad (5.a)$$
$$RSSD_{anc}(\theta_{tilt}) = G_T^{dB}(\theta_{tilt} - \beta) - G_T^{dB}(\theta_{tilt} + \beta) \quad (5.b)$$

The angular displacement, represented by β, explicitly affects $RSSD_{tag}$. However, its influence on the receiving antenna pattern is minor due to the tag's lower-directivity antennas. In contrast, the effect of β on the transmit antenna pattern is significant, which is analyzed in detail in Section III.

B. Theoretical validation of Adaptive Calibration method

Fig. 2 illustrates a general case where the anchor and tag exhibit misalignment by an angle θ_{tilt}. To accurately model this in a 2-D localization framework, we define additional angular parameters in Fig. 4(a). The anchor is assumed to be fixed at the origin, while the tag's relative position is described using the

AP2503-0890

positional angle θ_{pos} and the distance D. To account for the orientation of each device separately, misalignment angle θ_{tilt} is divided into two components: $\theta_{tilt,tag}$ and $\theta_{tilt,anc}$. The angle $\theta_{tilt,tag}$ represents the tag's orientation angle relative to z-axis, while $\theta_{tilt,anc}$ represents the anchor's orientation angle relative to the z-axis. As a result, for applicability to the general scenario illustrated in Fig. 4(a), Equation (4) is reformulated as follows:

$$\begin{aligned} RSSD_c\,(\theta_{inc}, \theta_{tilt}) &= RSSD_{tag}(\theta_{inc}) + RSSD_{anc}(\theta_{tilt}) \\ &= RSSD_{tag}(\theta_{pos} - \theta_{tilt,tag}) \\ &\quad + RSSD_{anc}(\theta_{pos} - \theta_{tilt,anc}) \end{aligned} \quad (6)$$

The angle $\theta_{tilt,tag}$ and $\theta_{tilt,anc}$ can be easily obtained using commonly available sensors in mobile devices, such as magnetic sensors.

To validate the effectiveness of (6), we conducted simulations using ANSYS HFSS, modeling realistic tag-anchor configurations, as illustrated in Fig. 4(a). Before leveraging the calibrated RSSD from (6) to estimate moving tag's position, a few simulations are conducted to obtain $RSSD_{tag}$ as a function of θ_{inc} and $RSSD_{anc}$ as a function of θ_{tilt}. To isolate individual effects, simulations are configured as in Fig.2 and conducted by varying θ_{inc} while fixing θ_{tilt} at 0° and vice versa.

To simulate the behavior of a mobile tag, the tag moves along the y-axis, with θ_{pos} varying from -80° to 80° in 5° steps. To avoid excessive simulations, which are time-consuming and require substantial computational resources, $\theta_{tilt,anc}$ is set to 0°,while $\theta_{tilt,tag}$ varies among 0°, 10°, 20°, 30°, 45°. The simulation results are represented as $RSSD_m$. Fig. 4(b) compares the calibrated $RSSD_c$, derived from (6), with the simulated $RSSD_m$, each represented by a solid line and scatters. Scenarios with the same $\theta_{tilt,tag}$ are represented using lines and scatter points of the same color. The estimated positional angle $\hat{\theta}_{pos}$ is determined as the angle that minimizes the difference between $RSSD_c$ and $RSSD_m$.

To avoid estimation errors caused by ambiguity on $RSSD_c$, the DoA estimation is conducted within the specific angular range named FoV, as previously mentioned. In this paper, the FoV is defined as a monotonous decreasing or increasing region around 0° [10]. Table I summarizes the Root-Mean-Square Error (RMSE) for DoA estimation with and without calibration. Equation (5.a) is used to generate "w/o calibration" in Table I while equation (4) is used for "w/ calibration". Our results confirm that the proposed calibration method significantly reduces errors—achieving a 12-fold improvement, from 12.31° (uncalibrated) to 1.01° at $\theta_{tilt,tag} = 0°$.

C. Experimental validation of adaptive Calibration method

We experimentally validate the proposed calibration method under real-world conditions. The mobile tag is configured with a tilted antenna array consisting of 1×2 patch arrays. This configuration was selected based on a systematic methodology detailed in our prior work [17], where the RSSD slope was established as a key performance metric correlating antenna design choice with DoA accuracy. Through this methodology, the 1×2 array was identified as an optimal design that
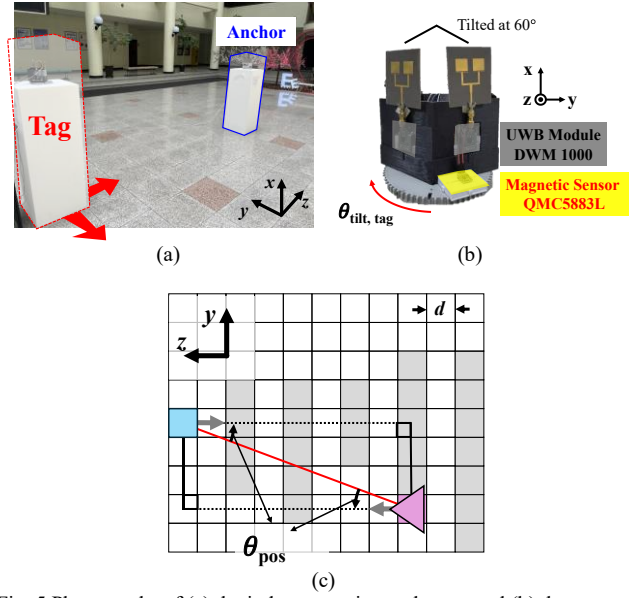

(a)

(b)

(c)

Fig. 5 Photographs of (a) the indoor experimental setup and (b) the proposed tag device used to verify the effectiveness of the proposed calibration method. (c) Measurement results comparing $RSSD_c$ and $RSSD_m$.
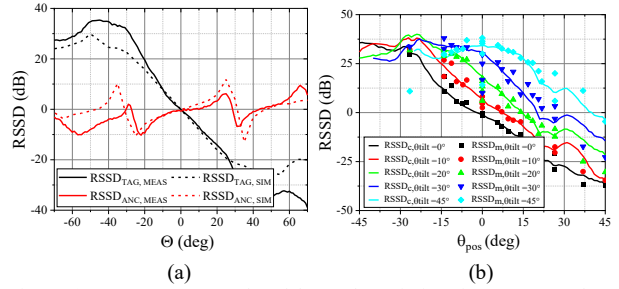

(a)

(b)

Fig. 6 (a) Measurement results of the angle variations in $RSSD_{tag}$ and $RSSD_{anc}$ and (b) comparison of calibrated $RSSD_c$ and measured $RSSD_m$.

TABLE II. EXPERIMENTAL-BASED ESTIMATION ERROR: RMSE COMPARISON (CALIBRATION VS. NO CALIBRATION, WITHIN FoV)

Estimation Error (°)	$\theta_{tilt,tag}$				
	0°	10°	20°	30°	45°
w/ Calibration	3.79	5.58	5.33	7.28	16.98
w/o Calibration	9.42	7.33	14.78	25.85	36.54

effectively balances estimation performance and physical constraints. The anchor uses a 1×4 patch array to ensure sufficient gain. For experimental implementation, the tag and anchor communicate via the UWB COTS module, Decawave DWM1000[21], supporting IEEE 802.15.4 IR-UWB communication; chosen for minimal indoor attenuation. Both the tag and anchor devices are equipped with QMC5883L magnetic compass modules to obtain relative orientation for adaptive calibration. Fig. 5(a) shows the schematic of the tag components.

Before evaluating the validity of the proposed calibration method using $RSSD_m$ derived from different positions, $RSSD_{tag}$ and $RSSD_{anc}$ data are collected. As conducted in the simulation, to establish $RSSD_{tag}$ and $RSSD_{anc}$, each device is rotated independently while keeping the other fixed. The variations as a function of the rotation angle θ are plotted in Fig. 6 (a). The

AP2503-0890

TABLE III. EXPERIMENTAL-BASED ESTIMATION ERROR: RMSE
COMPARISON (CALIBRATION VS. NO CALIBRATION, OUTSIDE-THE-FOV)

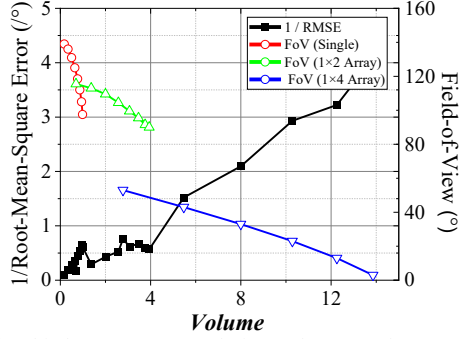| Estimation Error (°)	$\theta_{tilt,tag}$				
	0°	10°	20°	30°	45°
w/ Calibration	9.68	10.2	14.4	10.49	17.65
w/o Calibration	11.33	9.10	19.59	29.481	41.58

Fig. 7. Relationship between antenna design and DoA performance in terms of DoA accuracy and FoV.

dashed lines indicate simulation results, while the solid lines represent experimental results. Additionally, due to the magnetic sensor's sensitivity to metallic components, the bearing angle derived from the sensor is collected before evaluation. This helps compensate for distortion caused by metallic interference while varying the ground truth azimuth angle.

Similar to the simulation setup depicted in Fig. 4(a), the experimental environment is set up as shown in Fig. 5(a). Experiments conducted outside the anechoic chamber can demonstrate the feasibility of the proposed method in real-world environments. Mobile tag moves in the directions of the y and z-axes, with a step size of 45 cm, same as tile width. The common possible movement positions are limited to 25 points within the shaded areas of Fig. 5(b) due to the receiver's sensitivity. At each position, the tag's estimation process is conducted in four steps: (1) extracting data from received packets ($\theta_{tilt,anc}$ and RSSD$_m$), (2) deriving $\theta_{tilt,tag}$, (3) computing RSSD$_c$ by applying orientation angles, and (4) determining the estimated positional angle $\hat{\theta}_{pos}$.

Fig. 6(b) compares RSSD$_c$ represented by solid lines reflecting the ground-truth $\theta_{tilt,tag}$ with the measured RSSD$_m$ represented by scatter points, for different tag orientations. Similar to the simulation results in Table I, Table II shows experimental DoA estimation error for both calibrated and uncalibrated results. The table demonstrates significantly reduced errors in the calibrated results, despite the degradation in accuracy compared to simulations due to multipath effects and the reflective channel environment in real-world scenarios. Specifically, accuracy improves by a factor of 2.5 to 3.5 across all tilt angles. At θ_{tilt}=0°, calibration reduces RMSE from 9.42° to 3.79° a 2.5-fold improvement, demonstrating the method's effectiveness.

III. CAUSES OF LIMITED DoA PERFORMANCE

The proposed calibration process across different tag orientations has been validated in previous sections, demonstrating enhanced accuracy. However, in the previous section, to avoid ambiguity in RSSD variations with respect to the incident angle, DoA estimation was only conducted within a limited FoV, which is a critical performance metric. Furthermore, although accuracy improves across all tag orientations, larger θ_{tilt} values lead to increased estimation errors. The following section analyzes the key factors contributing to these limitations, focusing on the impact of FoV constraints and tilt-dependent errors.

A. Fundamental FoV Limitations on DoA estimation

To resolve ambiguity in RSSD-based DoA estimation, FoV constraints are generally introduced to ensure a unique mapping between RSSD values and incident angles. Within the FoV, each RSSD measurement corresponds to a single incident angle, eliminating potential estimation errors. Determining the estimated incident angle $\hat{\theta}_{inc}$ involves selecting the angle within the defined FoV range that minimizes the difference between the calibrated RSSD in (4) and the measured RSSD$_m$.

If the FoV is not defined in the estimation step, ambiguity between RSSD and the incident angle arises. This ambiguity leads to multiple estimated incident angle candidates, further reducing accuracy. Table II and III quantify the impact of FoV constraints on DoA estimation accuracy. Without FoV constraints, estimation errors in Table III increase significantly compared to those in Table II. Specifically, at θ_{tilt}=0°, the RMSE in Table III is approximately three times higher than in Table II. Although calibration reduces errors, the absence of an FoV constraint introduces multiple possible angle estimates, degrading accuracy.

However, to enable application in real-world scenarios, both high accuracy and a wide FoV must be ensured. To achieve this, the effect of tag design on DoA performance is studied. In typical tag designs using tilted array configurations, FoV and DoA estimation accuracy are determined by a tilted angle between two tag antennas and antenna directivity [22]. The effect of tag design on FoV and estimation accuracy is analyzed through multiple simulations with different tag configurations. The simulations cover 24 tag designs, varying across eight tilt angles (ranging from 10° to 80° in 10° increments) and three different antenna types: single antenna, 1×2 antenna array, and 1×4 antenna array.

As a result of a series of simulations, Fig. 7 illustrates the relationship between FoV, RMSE estimation errors, and antenna volume, which represents antenna design characteristics. Colored scattered lines indicate FoV variations across different antenna types: red represents tags using a single antenna, green represents a 1×2 antenna array, and blue represents a 1×4 antenna array. The black scattered line represents 1/RMSE, indicating estimation accuracy. In Fig. 7, as the antenna volume increases—resulting in higher directivity and a larger tilting angle—the FoV becomes narrower, while estimation accuracy improves. Disregarding the inapplicability
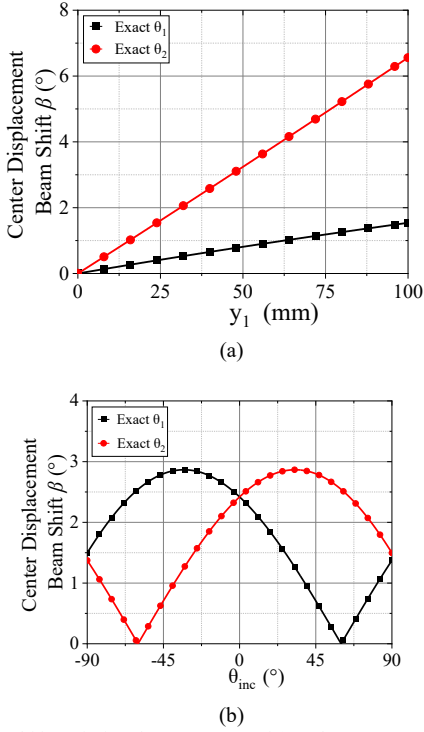
(a)

(b)

Fig. 8. Beam shift variation for Antenna 1 (θ_1) and Antenna 2 (θ_2) as a function of (a) the phase center of the tag antenna and (b) the incident angle.
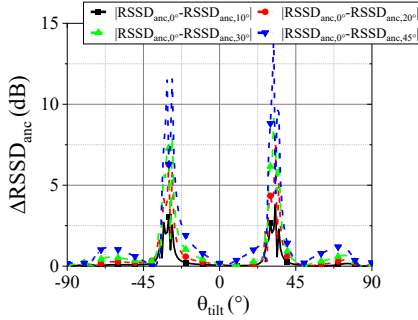

Fig. 9. RSSD errors caused by the assumption of a constant beam shift β.

of large antenna volumes in small tag devices, DoA accuracy and FoV exhibit a trade-off relationship, as observed in Fig. 7. This occurs because a narrow FoV enables higher sensitivity in DoA estimation. Consequently, a wide FoV and highly accurate DoA estimation are fundamentally incompatible.

B. The constant β effect on DoA estimation

Another major source of DoA estimation error arises from the assumption of a constant β to simplify calibration equation (4), treating the angles θ_1 and θ_2 in Fig. 3 as identical. However, beam shift angle θ_n in (3) varies based on the tag-anchor geometry and incident angle, leading to tilt-dependent errors. Consequently, estimation errors at $\theta_{tilt}=45°$ are five times larger than those at $\theta_{tilt}=0°$ in Table II.

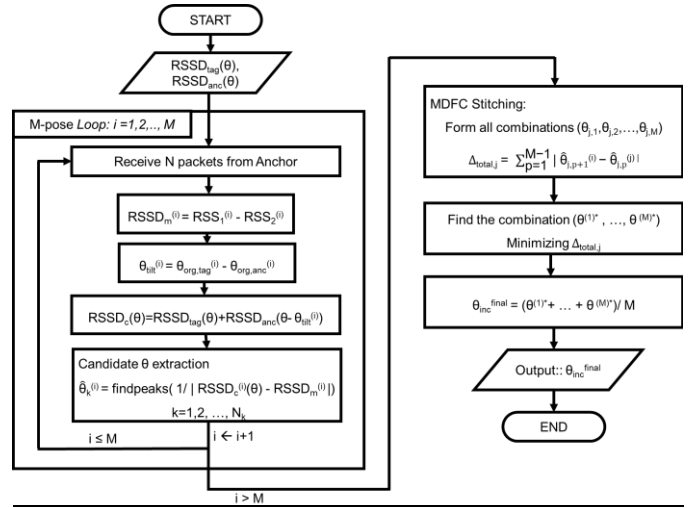To analyze the effects of beam shift angle variation on DoA

Fig. 10. Flowchart of Multi-pose FoV compensation scheme

estimation, it is necessary to derive the exact values of θ_1 and θ_2 and analyze their impact on RSSD. The exact values of θ_1 and θ_2 can be determined by a simple geometrical relationship between the anchor and tag, as shown in Fig. 3. In Fig. 3, the angle θ_1 is between the tag-anchor path and the first tag antenna's phase center-anchor path, while θ_2 is defined similarly for the second antenna. Following this relationship, the value of θ_1 and θ_2 is given by (7.a) and (7.b), as shown at the bottom of the page. Previously mentioned, y_1 and z_1 represent the phase center offsets of each antenna along the y-axis and z-axis, respectively. According to (7), it is obvious that θ_1 and θ_2 are influenced by the tag-anchor position and incident angle. Fig. 8(a) shows variations in the beam shift angle corresponding to different tag antenna positions along the y-axis. While z_1 is fixed at 50 mm, y_1 varies from 0 mm to 100 mm. Fig. 8(b) illustrates variations in the beam shift angle for different incident angles, ranging from -90° to 90°, with both y_1 and z_1 fixed at 50 mm. In Fig. 8, the angle θ_1 is represented by a black scattered line while the angle θ_2 is represented by a red scattered line. Obviously, as illustrated in Fig. 8, θ_1 and θ_2 are distinct and variable in most cases, contradicting the assumption established for deriving (4). Despite a constant β assumption, calibration method can enhance DoA estimation performance across all tilting angles, especially at $\theta_{tilt}=0°$.

In Sections II, $RSSD_{anc}$ are collected by rotating only the anchor while keeping the tag facing the anchor. In other words, $RSSD_{anc}$ is obtained under the assumption of a constant beam shift at $\theta_{inc}=0°$ and used for validations across all tilt angles. Consequently, large estimation errors are unavoidable for cases where $\theta_{inc}\neq0°$. Fig. 9 illustrates $RSSD_{anc}$ variations due to changes in θ_1 and θ_2 caused by variations in the incident angle. In detail, Fig. 9 represents the difference in $RSSD_{anc}$ between $\theta_{inc}=0°$ and other orientation cases. As the orientation angle

$$\theta_1 = \cos^{-1}\left(\frac{(\cos(\theta_{inc}))(D\cos(\theta_{inc})+z_1)+(\sin(\theta_{inc}))(D\sin(\theta_{inc})+y_1)}{\sqrt{(D\cos(\theta_{inc})+z_1)^2+(D\sin(\theta_{inc})+y_1)^2}}\right) \quad (7.a)$$

$$\theta_2 = \cos^{-1}\left(\frac{(\cos(\theta_{inc}))(D\cos(\theta_{inc})+z_1)+(\sin(\theta_{inc}))(D\sin(\theta_{inc})-y_1)}{\sqrt{(D\cos(\theta_{inc})+z_1)^2+(D\sin(\theta_{inc})-y_1)^2}}\right) \quad (7.b)$$
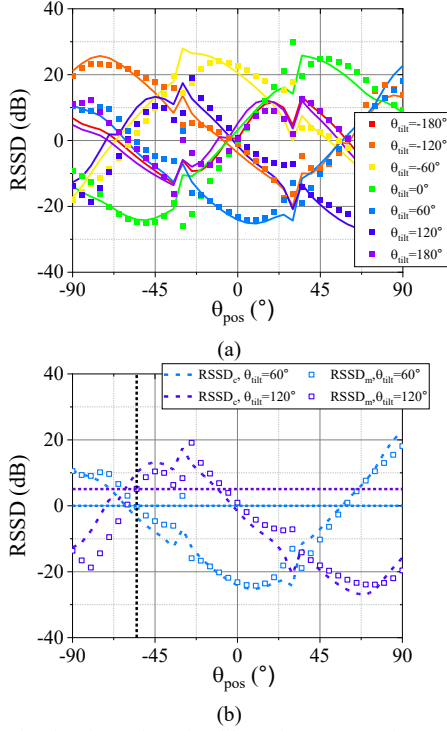
(a)

(b)

Fig. 11 (a) Simulated results of calibrated RSSD$_c$ and measured RSSD$_m$ obtained by rotating the tag in 60° steps and (b) an example of applying the MPFC scheme to DoA estimation results obtained at θ_{tilt}= 60° and 120°, shown in Fig.11 (a).

increases, the RSSD$_{anc}$ difference becomes more severe. These findings suggest that adaptive compensation for β variations is necessary for accurate DoA estimation in real-world scenarios. However, compensating for this angular variation is impractical, as it requires precise knowledge of the tag and anchor positions, along with the incident angle—parameters that themselves rely on the estimation process, leading to a cyclical dependency.

IV. MULTI-POSE FOV COMPENSATION (MPFC) SCHEME

As shown in the previous section, the FoV is determined by the antenna design and remains fixed, limiting the range of measurable incident angles. Additionally, due to the phase center mismatch between tag antennas, fundamental constraints limit DoA estimation accuracy. To overcome FoV constraints and tilt-dependent errors, we propose the Multi-Pose FoV Compensation (MPFC) method. This approach leverages multiple tag orientations to refine DoA estimation and merges the results. By integrating DoA estimates from different tag orientations, MPFC effectively extends the FoV while reducing estimation errors across a wider angular range. The entire process, from signal capture to the final DoA estimation, using MPFC scheme, is visually delineated in the flowchart in Fig. 10.

A. Introducing Multi-pose FoV Compensation Scheme

The mobile tag sensor moves freely and rotates according to the movement of the person holding the tag within a short time frame [23]. Thus, the same incident angle can naturally be observed across different tag orientations. In [24] and [25], while decentralized systems present challenges due to resource limitations, sensor mobility can mitigate these constraints,
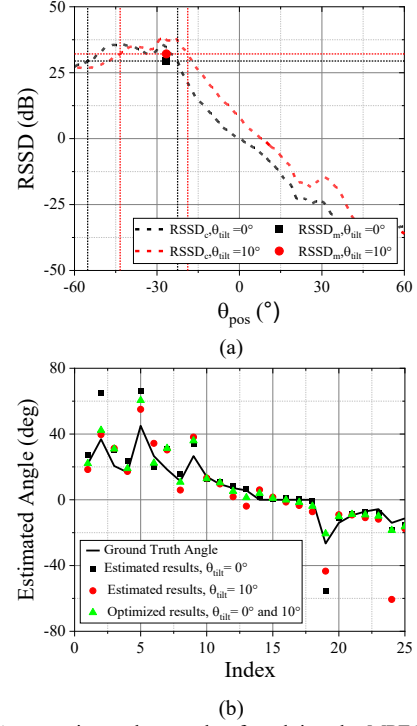

(a)

(b)

Fig. 12 (a) An experimental example of applying the MPFC scheme to DoA estimation results obtained at θ_{tilt}= 0° and 10°, measured under the setup shown in Fig. 4(a). (b) Compensated results obtained by combining both DoA estimation results using the MPFC scheme.

TABLE IV. ESTIMATION ERROR USING MPFC SCHEME: RMSE COMPARISON (CALIBRATION VS. NO CALIBRATION)

Estimation Error (°)		$\theta_{tilt}^{(2)}$			
		10°	20°	30°	45°
$\theta_{tilt}^{(1)}$	0°	5.57	7.88	5.54	12
	10°		9.19	6.18	13.54
	20°			7.66	14.40
	30°				10.51

enhancing estimation accuracy through dynamic adjustments and increased measurement diversity. Similarly, to address ambiguity issues in calibrated RSSD$_c$ for a typical mobile tag, the proposed MPFC method utilizes RSSD values collected from multiple orientations while maintaining the same position. Since solutions derived from different orientations converge to the common solution for RSSD values, this approach eliminates ambiguity and enhances accuracy.

Fig. 11 (a) presents the calibrated RSSD$_c$ and RSSD$_m$ for seven different tag orientations, using ANSYS SBR simulations to model realistic signal propagation. The solid lines represent the expected calibrated RSSD$_c$ curve, while scatter points denote actual simulated measurements RSSD$_m$. For a more detailed explanation of MPFC operation, Fig. 11 (b) is introduced, illustrating RSSD$_c$ variations with respect to θ_{pos} for different orientations, θ_{tilt}=60° and 120°. As shown in Fig. 11 (b), a single RSSD$_c$ curve may yield multiple candidate angles, leading to errors. However, by integrating measurement results

AP2503-0890

TABLE V. ESTIMATION ERROR FOR
FOUR METHODS UNDER VARYING TAG TILT ANGLES

θ_{tilt} / Method	0°	10°	20°	30°	45°
S/D	23.32°	19.54°	16.29°	14.44°	18.75°
S/D+MPFC	-	27.65°	28.1°	16.91°	20.73°
Calibrated RSSD	9.68°	10.2°	14.4°	10.49°	17.65°
Cal. MPFC	-	5.57°	7.88°	5.54°	12°

TABLE VI. COMPARISON WITH DoA SENSORS IN RELATED WORKS

	[16]	[8]	[18]	[14]	This Work
DoA Estimation Method	PDPC*	PPCC†	S-D‡	S-D‡	Difference-only
# of Antennas	8	12	1	2	2
Effective FoV (°)	360	360	180	50	180§
FoV per Antenna Mode (°)	45	30	8.18	25	90
Full DoA Coverage	Yes	Yes	No	No	Yes
Orientation Robustness	No	No	No	No	Yes
Estimation Error (RMSE, °)	24	7.9	14	<2	5.57 $\theta_{tilt}^{(1)}$=0°, $\theta_{tilt}^{(2)}$=10°
Mobile Tag Scenario	Yes	No	No	Yes	Yes

*PDPC: Phase Difference Profile Calculation
† PPCC: Power-Pattern Cross-Correlation algorithm
‡ S-D: Sum-Difference method
§ With a fixed anchor orientation, the positional angle θ_{pos} expands from -90° and 90°, effectively covering the full angular range of possible tag positions.

from different orientations, MPFC mitigates the aforementioned ambiguity issues that lead to multiple candidates. Illustrated in Fig. 11 (b), both calibrated $RSSD_c$ curves varying with θ_{pos} have identical solution, leading to accurate DoA estimation results, despite slight discrepancies due to the constant β assumption. In other words, MPFC ensures that the common solution converges to the correct incident angle, enhancing accuracy while maintaining low hardware complexity.

Empirically, the effectiveness of the MPFC scheme can be verified, using the same dataset measured in Fig. 4 (b). Fig. 12 (a) presents both $RSSD_c$ and $RSSD_m$ measurements for $\theta_{tilt} = 0°$ and 10° when θ_{pos} = -26.56°. The black line and scatter points represent $\theta_{tilt} = 0°$, while the red ones correspond to $\theta_{tilt} = 10°$. Each $RSSD_c$ derives the estimated angle candidates $\hat{\theta}_{inc,1}$ and $\hat{\theta}_{inc,2}$, depicted as colored dashed x-lines where $\hat{\theta}_{inc,1} < \hat{\theta}_{inc,2}$. Ideally, either $\hat{\theta}_{inc,1}$ and $\hat{\theta}_{inc,2}$ for $\theta_{tilt}= 0°$, and either $\hat{\theta}_{inc,1}$ and $\hat{\theta}_{inc,2}$ for $\theta_{tilt}= 10°$, should converge to a common solution as shown in Fig.11 (b). However, due to experimental errors in $RSSD_m$, the solutions may not converge perfectly.

In such cases, $\hat{\theta}_{inc}$ is approximated by averaging the two closest solutions derived from the respective orientations. In Fig. 12 (a), the possible solutions for the measured RSSD are -22.5° and -55.2° for $\theta_{tilt} = 0°$, and -18.8° and -43.4° for $\theta_{tilt} = 10°$. Among the four solutions illustrated in Fig. 12 (a), $\hat{\theta}_{inc,2}$ for $\theta_{tilt}= 0°$ and 10° are selected due to their close proximity- -22.5° and -18.8° for $\theta_{tilt} = 0°$ and 10°, respectively. Finally, by averaging the two closest values, the final estimated incident angle is determined as -20.65°.

To further demonstrate the validity of the proposed scheme at different positions in a real-world scenario, Fig. 12 (b) presents the whole estimation results using measured data in Fig. 4(b). The ground truth incident angle is represented by black lines, while the estimated angles using $_{tilt} = 0°$ and $\theta_{tilt} = 10°$, and both orientations are marked by different colored scatter points. When both orientations are utilized, the estimated angles align more closely with the ground truth compared to a single orientation, demonstrating improved accuracy. Furthermore, Table IV demonstrates the estimation results using the RSSD values from two different tag orientations, denoted as $\theta_{tilt}^{(1)}$ and $\theta_{tilt}^{(2)}$ ($\theta_{tilt}^{(1)} < \theta_{tilt}^{(2)}$). The MPFC scheme significantly improves DoA estimation accuracy across all test cases, reducing RMSE by nearly 50% compared to Table III. Compared to

conventional multi-antenna methods, MPFC achieves this improvement without requiring additional hardware, making it a practical solution for resource-constrained mobile tags.

B. Comparison with the related works

To evaluate the performance and demonstrate the significance of our proposed method, we conducted a benchmark comparison against conventional techniques under identical experimental conditions. Using the same measured RSS dataset, we evaluated three key approaches: (1) the classical monopulse sum-and-difference (S/D) method, (2) the S/D method augmented with our MPFC scheme (S/D+MPFC), and (3) our proposed approach combining adaptive calibration with MPFC (Cal. MPFC). The DoA estimation errors for each method across varying tag tilt angles are summarized in Table V. For the methods involving MPFC, the first measurement is assumed to be at the reference orientation, $\theta_{tilt}^{(1)}=0°$.

The results in Table V clearly show that the conventional S/D method, lacking proper calibration for tag tilt, exhibits large errors of 14°–23°. Furthermore, simply applying MPFC to this uncalibrated method increases the error to ~20°. This occurs because the uncalibrated S/D curve deforms unpredictably with tilt and saturates at certain incident angles, creating fundamental ambiguity that MPFC cannot resolve. This conclusively demonstrates that our proposed adaptive calibration is an essential prerequisite for MPFC to function effectively. Ultimately, their combination achieves a four-fold improvement in accuracy compared to the conventional S/D method.

Table VI presents a comparative analysis of the proposed MPFC method against existing DoA estimation techniques, focusing on key performance metrics including estimation

AP2503-0890

accuracy, effective FoV, system complexity, and application scalability. For consistency, the MPFC results are evaluated using two representative tag orientations, $\theta_{tilt}^{(1)}=0°$ and $\theta_{tilt}^{(2)}=10°$. Prior works in [8] and [16] attempt to cover a full DoA coverage by employing a large number of antennas; however, this approach suffers from substantial hardware complexity. In contrast, [18] reports a 180° FoV using a single frequency-scanning antenna; however, its performance is constrained by the finite number of radiation modes (22 modes) and susceptibility to channel interference.

The proposed MPFC scheme achieves full DoA estimation coverage by compensating for orientation-dependent FoV limitations, using only two antennas. This enables a FoV-per-antenna-mode ratio of 90°, significantly improving angular coverage efficiency without introducing interference or requiring additional hardware. As a result, MPFC achieves efficient DoA estimation across a wide angular range while drastically reducing hardware complexity.

Furthermore, MPFC calibrates and compensates for tilt-dependent errors, which have not been explicitly considered in previous work. For example, the study in [14] attempted to improve DoA performance by adjusting anchor orientation and reported an error below 2°, while it lacked a systematic analysis of performance-limiting factors. In contrast, the proposed method incorporates an adaptive orientation-aware calibration process to mitigate the impact of tag-anchor misalignment and validates its effectiveness through real-world experiments. While [14] achieves the lowest error in an outdoor setting with a limited 50° FoV, the proposed approach attains an RMSE of 5.57° in real-world indoor scenarios, achieving full DoA coverage without the need for additional external systems.

Overall, MPFC enhances estimation accuracy while minimizing hardware complexity, making it a practical and scalable solution for mobile tag-based localization. By leveraging multiple orientations and RSSD-based calibration, it effectively balances accuracy, computational efficiency, and scalability for real-world applications.

V. CONCLUSION

We proposed an adaptive calibration method to correct misalignment errors in mobile tag-based DoA estimation under limited FoV situations. Our RSSD-based approach simplifies the estimation process while significantly improving accuracy. Experimental evaluations demonstrate that the proposed calibration method significantly reduces estimation errors from 9.42° to 3.79° under real-world conditions. Building on this foundation, we introduced the Multi-Pose FoV Compensation (MPFC) scheme, which extends the effective Field-of-View and achieves full DoA coverage by leveraging multiple tag orientations. By incorporating RSSD measurements from multiple tag orientations, MPFC mitigates tilt-dependent errors and eliminates estimation ambiguity. Our experimental results demonstrate that MPFC achieves up to a 60% reduction in RMSE compared to traditional single-orientation methods. Compared to conventional DoA estimation methods that rely on large antenna arrays, MPFC achieves high accuracy with minimal hardware—requiring only two antennas—resulting in a power-efficient and cost-effective localization system. Moreover, MPFC attains a FoV-per-antenna-mode ratio of 90°, representing superior angular efficiency per antenna resource. The proposed MPFC method offers a scalable solution for decentralized localization, particularly in IoT and healthcare applications. Future work will be directed towards real-time deployment, enhancing robustness in multi-tag environments, and extending the framework to three-dimensional localization, thereby broadening its overall applicability.

REFERENCES

[1] F. Zafari, A. Gkelias, and K. K. Leung, "A survey of indoor localization systems and technologies," *IEEE Commun. Surv. Tutor.,* vol. 21, no. 3, pp. 2568-2599, 2019.

[2] N. Bulusu, D. Estrin, L. Girod, and J. Heidemann, "Scalable coordination for wireless sensor networks: self-configuring localization systems," in *International Symposium on Communication Theory and Applications (ISCTA 2001), Ambleside, UK*, 2001, vol. 12: Citeseer.

[3] M. Tarkowski and L. Kulas, "RSS-based DoA estimation for ESPAR antennas using support vector machine," *IEEE Antennas Wireless Propag. Lett.,* vol. 18, no. 4, pp. 561-565, 2019.

[4] A. Yassin *et al.*, "Recent advances in indoor localization: A survey on theoretical approaches and applications," *IEEE Commun. Surv. Tutor.,* vol. 19, no. 2, pp. 1327-1346, 2016.

[5] A. Shastri *et al.*, "A review of millimeter wave device-based localization and device-free sensing technologies and applications," *IEEE Commun. Surv. Tutor.s,* vol. 24, no. 3, pp. 1708-1749, 2022.

[6] M. G. Rabbat and R. D. Nowak, "Decentralized source localization and tracking [wireless sensor networks]," in *2004 IEEE International Conference on Acoustics, Speech, and Signal Processing*, 2004, vol. 3: IEEE, pp. iii-921.

[7] Z. Kasmi, N. Guerchali, A. Norrdine, and J. H. Schiller, "Algorithms and position optimization for a decentralized localization platform based on resource-constrained devices," *IEEE Trans. Mobile Comput.,* vol. 18, no. 8, pp. 1731-1744, 2018.

[8] M. Groth, M. Rzymowski, K. Nyka, and L. Kulas, "ESPAR antenna-based WSN node with DoA estimation capability," *IEEE Access,* vol. 8, pp. 91435-91447, 2020.

[9] J. L. Gómez-Tornero, D. Cañete-Rebenaque, J. A. López-Pastor, and A. S. Martínez-Sala, "Hybrid analog-digital processing system for amplitude-monopulse RSSI-based MIMO WiFi direction-of-arrival estimation," *IEEE J. Sel. Top. Signal Process.,* vol. 12, no. 3, pp. 529-540, 2018.

[10] A. Cidronali, S. Maddio, G. Giorgetti, and G. Manes, "Analysis and performance of a smart antenna for 2.45-GHz single-anchor indoor positioning," *IEEE Trans. Microw. Theory Tech.,* vol. 58, no. 1, pp. 21-31, 2009.

[11] Q. Chen, H. Liu, M. Yu, and H. Guo, "RSSI ranging model and 3D indoor positioning with ZigBee network," in *Proceedings of the 2012 IEEE/ION Position, Location and Navigation Symposium*, 2012: IEEE, pp. 1233-1239.

[12] M. Betke and L. Gurvits, "Mobile robot localization using landmarks," *IEEE Trans. Robot. Autom.,* vol. 13, no. 2, pp. 251-263, 1997.

[13] O. Jean and A. J. Weiss, "Geolocation by direction of arrival using arrays with unknown orientation," *IEEE Trans. Signal Process.,* vol. 62, no. 12, pp. 3135-3142, 2014.

[14] S.-Y. Huang and R.-B. Wu, "Positioning for search and rescue in GPS-denied area by distributed WiFi RSS-based DoA modules," *IEEE Access,* vol. 10, pp. 76105-76113, 2022.

[15] S. Lian, J. Wang, B. Zhang, W. Meng, and F. Zhang, "Full Coverage 3D Indoor Positioning System Based on a Rotating dual-Ultra-Wide-Band Platform," *IEEE Trans. Instrum. Meas.,* 2025.

[16] N. Paulino and L. M. Pessoa, "Self-localization via circular bluetooth 5.1 antenna array receiver," *IEEE Access,* vol. 11, pp. 365-395, 2022.

[17] J. Werner, J. Wang, A. Hakkarainen, D. Cabric, and M. Valkama, "Performance and Cramer−Rao bounds for DoA/RSS estimation and transmitter localization using sectorized antennas," *IEEE Trans. Veh. Technol.,* vol. 65, no. 5, pp. 3255-3270, 2015.

[18] A. Gil-Martínez, M. Poveda-García, J. A. López-Pastor, J. C. Sánchez-Aarnoutse, and J. L. Gómez-Tornero, "Wi-Fi direction finding with frequency-scanned antenna and channel-hopping scheme," *IEEE Sensors J.,* vol. 22, no. 6, pp. 5210-5222, 2021.

[19] M. Kim and W. Hong, "Correlating Mobile Antenna Topologies with Received Signal Strength-based Direction-of-Arrival Estimation Method for Sub-Degree Accuracy within Indoor Environments," in *2024 IEEE International Symposium on Antennas and Propagation and INC/USNC-URSI Radio Science Meeting (AP-S/INC-USNC-URSI)*, 2024: IEEE, pp. 475-476.

[20] S. Maddio, A. Cidronali, M. Passafiume, G. Collodi, M. Lucarelli, and S. Maurri, "Multipath robust azimuthal direction of arrival estimation in dual-band 2.45–5.2 GHz networks," *IEEE Trans. Microw. Theory Tech.,* vol. 65, no. 11, pp. 4438-4449, 2017.

[21] "DWM1000 Datasheet," Version 1.4.

[22] S. M. Sherman and D. K. Barton, *Monopulse principles and techniques*. Artech House, 2011.

[23] W.-T. Shih, C.-K. Wen, S.-H. Tsai, R. Liu, and C. Yuen, "EasyAPPos: Positioning Wi-Fi access points by using a mobile phone," *IEEE Internet Things J.,* vol. 10, no. 15, pp. 13385-13400, 2023.

[24] D. Jeong and K. Lee, "Directional RSS-based localization for multi-robot applications," in *Proceedings of WSEAS conf. on signal processing, robotics, and automation*, 2013.

[25] Z. Gong *et al.*, "Design, analysis, and field testing of an innovative drone-assisted zero-configuration localization framework for wireless sensor networks," *IEEE Trans. Veh. Technol.,* vol. 66, no. 11, pp. 10322-10335, 2017.